Gadolinium-implanted GaN studied by spin-polarized positron annihilation spectroscopy

M. Maekawa, A. Miyashita, S. Sakai, and A. Kawasuso*

National Institutes for Quantum and Radiological Science and Technology, 1233, Watanuki, Takasaki, Gunma 370-1292, Japan

(Received 25 March 2020; revised 23 July 2020; accepted 6 August 2020; published 19 August 2020)

In this study, Gd ion implantation and annealing were performed at 900° C for nominally undoped wurtzite GaN grown by metal-organic chemical vapor deposition. Spin-polarized positron annihilation measurements showed that vacancy clusters including at least 12 vacancies per cluster were the major positron-trapping centers and that the electrons in the vacancy clusters were spin-polarized. These observations could be explained by first-principles calculations. The previous speculation about the defect-assisted ferromagnetism of Gd-implanted GaN may be supported if vacancy clusters are considered.

DOI: 10.1103/PhysRevB.102.054427

I. INTRODUCTION

The synthesis of dilute magnetic semiconductors is a key technology toward semiconductor spintronics. A successful dilute magnetic semiconductor is Mn-doped *p*-type GaAs and InAs with a Curie temperature of 180 K [1–3]. Furthermore, it was predicted theoretically that doping Mn into GaN and ZnO will result in a high Curie temperature (i.e., above 300 K) due to a high hole concentration of 10^{20} cm^{-3} [4]. However, Mn-doping into GaN seems to be very problematic due to the formation of secondary phases, and carrier-mediated ferromagnetism by this method remains controversial.

Meanwhile, in 2002, Teraguchi *et al.* [5] demonstrated the room-temperature ferromagnetism of Gd-doped GaN grown by molecular beam epitaxy, showing that the secondary phase formation is suppressed well. Thereafter, several groups reported not only room-temperature ferromagnetism, but also colossal ferromagnetism in Gd-doped GaN during crystal growth [6–8] and Gd-implanted GaN [9–15]. Here, "colossal" ferromagnetism means that the magnetization per an introduced Gd atom far exceeds 7 μ_B, which is the intrinsic magnetization of a Gd atom. From comparisons among implanted elements, the presence of Gd atoms is thought to be crucial for the appearance of ferromagnetism [14].

In the above studies, hysteresis loops observed by superconducting quantum interference device (SQUID) magnetometry were considered to be the evidence of ferromagnetism. However, the SQUID magnetometry creates serious artifacts via the pinning of magnetic flux [16,17]. To prove the existence of ferromagnetism, some methods with elemental specificity were required. The hard x-ray absorption spectroscopy studies showed that Gd atoms are only paramagnetic and the spin polarization of Ga atoms is almost null [18–20]. Therefore, some defect species and oxygen impurities are thought to give rise to the magnetic order. Then, it has been proposed that single Ga vacancies and Ga vacancy-oxygen complexes are the source of ferromagnetism [21–23]: an electrically neutral Ga vacancy has a magnetic moment of 3 μ_B, and multiple moments can be coupled ferromagnetically with those of Gd atoms [24,25]. It is thought that only positron annihilation spectroscopy (PAS) can confirm such a hypothesis. However, a previous study in 2011 implied that there was only a poor correlation between the ferromagnetism of Gd-doped GaN and single Ga vacancies [26], but since then there have been no further investigations in that direction.

To confirm the existence of vacancy-assisted magnetism, it is important to detect the spin polarization associated with vacancies. Using spin-polarized PAS (SP-PAS), we showed previously that spin-polarized cation vacancies may assist the ferromagnetism of oxygen-irradiated ZnO [27]. In this study, we used SP-PAS to investigate Gd-implanted GaN. We found that instead of single Ga vacancies, vacancy clusters including at least 12 vacancies per cluster form during post-implantation annealing, and the electrons therein are spin-polarized.

II. EXPERIMENT

The samples were cut from a nominally undoped wurtzite GaN(0001) film (2-μm thick) that was grown by metal-organic chemical vapor deposition (MOCVD) on Al_2O_3(0001) and purchased from POWDEC K.K. These were implanted with 370-keV Gd ions to the maximum dose (ϕ) of 10^{16} Gd$^+$/cm^2. Using the SRIM code [28], the Gd concentration at the mean range (∼70 nm) was simulated to be approximately $\phi \times 1.5 \times 10^5$ cm^{-1} (i.e., 1.5×10^{20} Gd/cm^3 for $\phi = 10^{15}$ Gd$^+$/cm^2). After implantation, annealing was performed in a N_2 atmosphere for 30 min at 900° C, which has been reported to be the optimum annealing temperature [10]. X-ray diffraction (XRD) structural analysis was performed in the θ-2θ orientation using a RIGAKU SmartLab diffractometer without Ge(220) monochromators. Magnetization measurements were performed using a Quantum Design MPMS SQUID apparatus from 10 to 300 K. In each M–H curve, the diamagnetic linear background was subtracted. M–T curves were obtained in both zero-field and field-cooling conditions at 200 Oe. Conventional PAS based on the Doppler broadening of annihilation radiation (DBAR) method was performed

*Corresponding author: kawasuso.atsuo@qst.go.jp

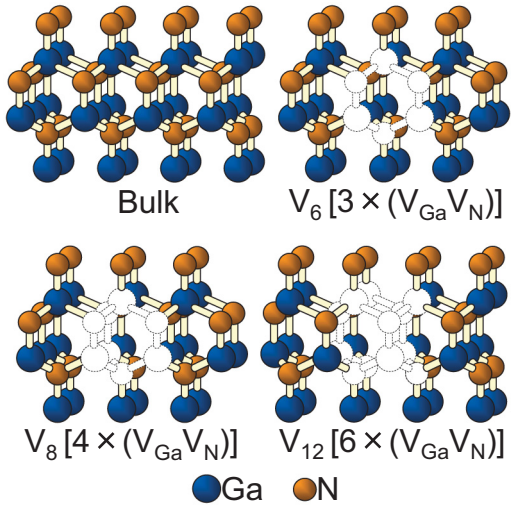

FIG. 1. Schematic representations of vacancy clusters considered in the calculation. The filled circles represent Ga and N atoms. The open circles represent vacancies.

with incident positron energy (E_+) of 2–15 keV at 300 K. As an index of the presence of vacancy defects, the line-shape S parameter, which is defined as the peak area intensity of the DBAR spectrum (i.e., 511 ± 1 keV) was determined. Also, coincidence-mode DBAR spectra were obtained for selected samples. Magnetic DBAR (MDB) measurements were performed using a longitudinally spin-polarized positron beam with a polarization of 27% in an out-of-plane magnetic field of 0.91 T at 20 and 300 K. Also obtained were the differential spectra $N_+(p) - N_-(p)$, where the subscripts + and − denote positive and negative magnetic fields, respectively, with respect to the positron spin polarization. The MDB intensity is defined as the total area of the differential spectrum. The details are described elsewhere [27].

III. THEORETICAL CALCULATIONS

To interpret the experimental results, calculations based on density functional theory (DFT) were performed within the generalized gradient approximation [29]. The valence electron wave functions were calculated using the projector augmented-wave method [30] with the ABINIT8.10.3 code [31]. The valence electron configurations were $3d^{10}4s^24p^1$, $2s^22p^3$, and $4f^75s^25p^65d^16s^2$ for Ga, N, and Gd atoms, respectively. For Gd, the Hubbard U correction (DFT + U) was considered with $U = 6.7$ eV and $J = 0.7$ eV [24,25]. Supercells including 64 and 128 atoms that correspond to $2 \times 2 \times 2$ and $4 \times 2 \times 2$ conventional wurtzite unit cells, respectively, were constructed. These systems with one Gd atom correspond to Gd contents of approximately 3 and 2 at. %, respectively. In addition to a perfect lattice, single N and Ga vacancies (V_N, V_{Ga}) and divacancy ($V_{Ga}V_N$) with $2 \times 2 \times 2$ cell, and 6-vacancy (V_6), 8-vacancy (V_8), and 12-vacancy (V_{12}) clusters with $4 \times 2 \times 2$ cell were examined. The configurations are shown schematically in Fig. 1. Note that the vacancy "cluster" does not mean the group of isolated Ga vacancies [32], but corresponds to the void geometry including both Ga and N vacancies. In all the calculations, the experimental lattice constants were used and the atomic positions were optimized in accordance with the molecular dynamics simulation installed in the code. The cutoff energy of the plane-wave basis set was 544 eV. The core electron wave functions were represented by the Slater function parameterized by Clementi and Roetti [33]. A self-consistent positron wave function was calculated based on the two-component DFT to minimize the energy functional [34]. The Borónski-Nieminen enhancement factor was adopted. The DBAR spectra were obtained by convoluting the one-dimensional angular correlation of the annihilation radiation spectra obtained from the momentum density with the Gaussian resolution function having a half width of 3.92×10^{-3} m_0c.

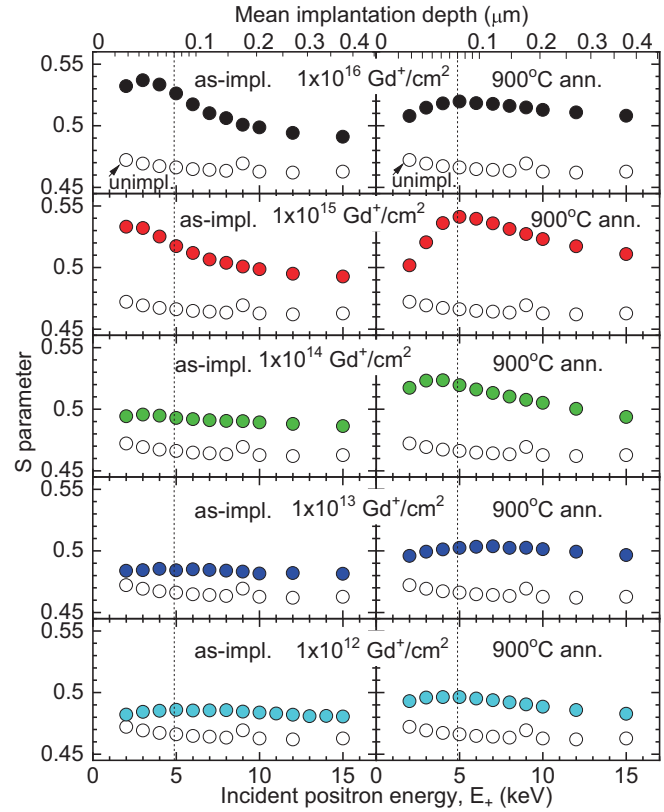

FIG. 2. Positron annihilation S parameter versus incident positron energy (S–E) plots measured at 300 K for the Gd-implanted samples before and after annealing at 900° C for 30 min (filled circles) and for the unimplanted sample (open circles). The upper horizontal axes show the mean positron implantation depth. Dashed lines denote the mean Gd range.

IV. RESULTS

A. Defect characterization by PAS and XRD

Figure 2 shows plots of the S parameter versus the incident positron energy (S–E plots) for the unimplanted sample and all the implanted samples before and after annealing at 900° C. The mean positron implantation depth is shown as the top horizontal axes. In the as-implanted states, the S parameter keeps low values at $\phi \leqslant 10^{13}$ Gd^+/cm^2, but starts to increase from

$\phi = 10^{14}$ Gd^+/cm^2. For $\phi \geqslant 10^{15}$ Gd^+/cm^2, the increase in the S parameter is more pronounced at $E_+ \leqslant 3$ keV. These indicate that small vacancies are introduced in the low dose conditions. The average S parameter for $\phi = 10^{12}$ Gd^+/cm^2 relative to the bulk value is ∼1.043. This is compatible with the theoretical value for single Ga vacancy (1.046). Although single N vacancies may also be created, the S parameter is theoretically very close to the bulk value and these are hardly detected. In the high dose conditions, larger vacancy clusters seem to be created. The pronounced vacancy production at $E_+ \leqslant 3$ keV is consistent with the SRIM simulation predicting a vacancy profile in a region that is a little shallower than the mean Gd range (∼70 nm). Figure 2 also shows that vacancy defects are created even in the deeper region up to 400 nm, which is much deeper than the simulated maximum Gd range (∼150 nm). Possible reasons for this might be the diffusion of created vacancy defects and/or the cascade damage due to recoiled atoms with channeling.

After annealing at 900° C, the pronounced increase in the S parameter at $E_+ \leqslant 3$ keV observed for $\phi \geqslant 10^{15}$ Gd^+/cm^2 vanishes. For $\phi = 10^{15}$ Gd^+/cm^2, a bump appears near the Gd range ($E_+ \sim 5$ keV), while such a bump is not appreciable for $\phi = 10^{16}$ Gd^+/cm^2. The S parameter for $\phi \leqslant 10^{14}$ Gd^+/cm^2 also increases upon annealing. These results indicate that upon annealing, the initial vacancy defects created by implantation are transformed into large vacancy clusters. The formation of vacancy clusters is enhanced with increasing dose up to $\phi = 10^{15}$ Gd^+/cm^2, but any further increase of dose is not efficient.

Figure 3 shows the so-called ratio DBAR spectra $N(p)/N_{ref}(p)$ for some selected samples before and after annealing at 900° C. Here, $N_{ref}(p)$ denotes the reference DBAR spectrum given by the unimplanted sample. In the as-implanted state, the spectrum for $\phi = 10^{12}$ Gd^+/cm^2 is in good agreement with the theoretical curve for single Ga vacancy (V_{Ga}). While, the spectrum for $\phi = 10^{16}$ Gd^+/cm^2 is significantly changed, i.e., the intensity in the low-momentum region greatly increases. The spectrum shape is compatible to the theoretical curve for 12-vacancy cluster (V_{12}). After annealing, the spectrum for $\phi = 10^{15}$ Gd^+/cm^2 is also in good agreement with the theoretical one for V_{12}. For $\phi = 10^{12}$ Gd^+/cm^2, the intensity in the low-momentum region is suppressed compared to that for $\phi = 10^{15}$ Gd^+/cm^2, but the curve shape itself does not change appreciably. To reproduce the experimental spectrum with the theoretical curve for V_{12}, the positron trapping fraction of 40% (described as the amplitude adjustment in Fig. 3) is required. Similarly, the experimental spectrum for $\phi = 10^{12}$ Gd^+/cm^2 is reproduced by V_6 with 50% trapping fraction and by V_8 with 60% trapping fraction, respectively. As discussed later, V_{12} with the positron trapping fraction of 40% can explain the dose dependence of effective magnetization. These again confirm that small vacancies such as single Ga vacancies are predominant for the as-implanted low-dose conditions. Also, these results leave no doubt about the formation of large vacancy clusters in the high-dose conditions and/or upon annealing. The average open volume of the detected vacancy clusters is comparable to that of V_{12}.

The calculations were also performed with Gd decoration of vacancy defects. It was found that replacing one of the nearest-neighbor Ga atoms around the V_{12} cluster with a Gd atom causes no distinct changes in the spectra without Gd decoration. Therefore, it is difficult to judge if the vacancy clusters are decorated with Gd atoms or not.

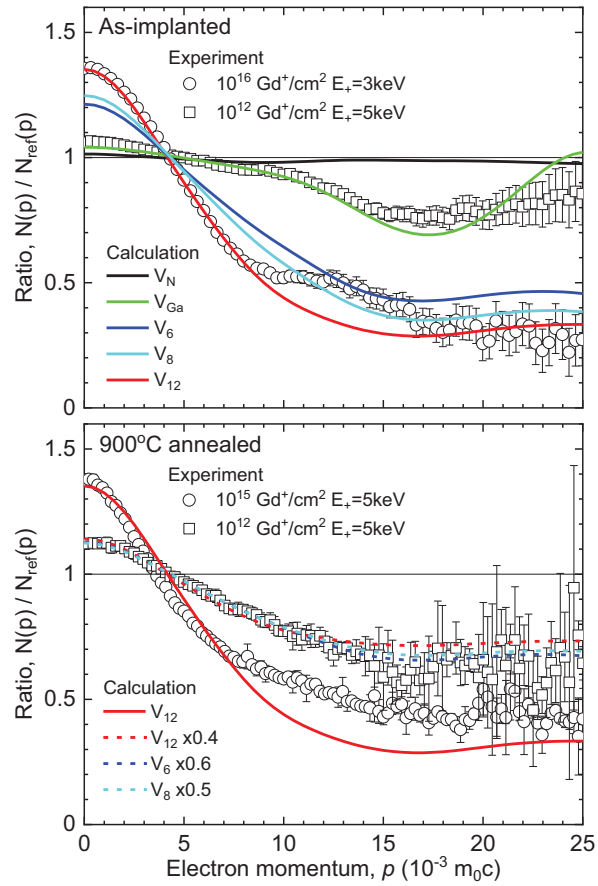

FIG. 3. The Doppler broadening of annihilation radiation (ratio) spectra at 300 K for the samples with doses of 10^{16} Gd^+/cm^2 (open circles) and 10^{12} Gd^+/cm^2 (open squares) in the as-implanted states (upper panel) and with doses of 10^{15} Gd^+/cm^2 (open circles) and 10^{12} Gd^+/cm^2 (open squares) after annealing at 900° C for 30 min (lower panel). The solid curves denote the theoretical calculations assuming V_N (black), V_{Ga} (green), V_6 (blue), V_8 (sky blue) and V_{12} (red). The broken lines are for V_6 (blue), V_8 (sky blue), and V_{12} (red) with the amplitude adjustments of 0.6, 0.5, and 0.4, respectively.

Figure 4 shows the XRD spectra obtained for the unimplanted sample and the implanted samples with $\phi = 10^{12}$ and 10^{16} Gd^+/cm^2 after annealing at 900° C. Only the reflections related to GaN and sapphire substrate are seen and the secondary phases such as metal Gd (32.4°) and GdN (30.9°) are absent. However, the formation of GaGdN phase (34.1°) is also not seen. The full width of half maximum (FWHM) of GaN(0002) reflection is 0.058° for the unimplanted sample and the implanted sample with $\phi = 10^{12}$ Gd^+/cm^2. This is even better than that of Si(111) reflection (0.065°) measured as a reference, suggesting that the crystallinity is maintained in the low-dose condition. For the sample with $\phi = 10^{16}$ Gd^+/cm^2, the FWHM is 0.083°, suggesting that defective structures are developed with increasing Gd dose.

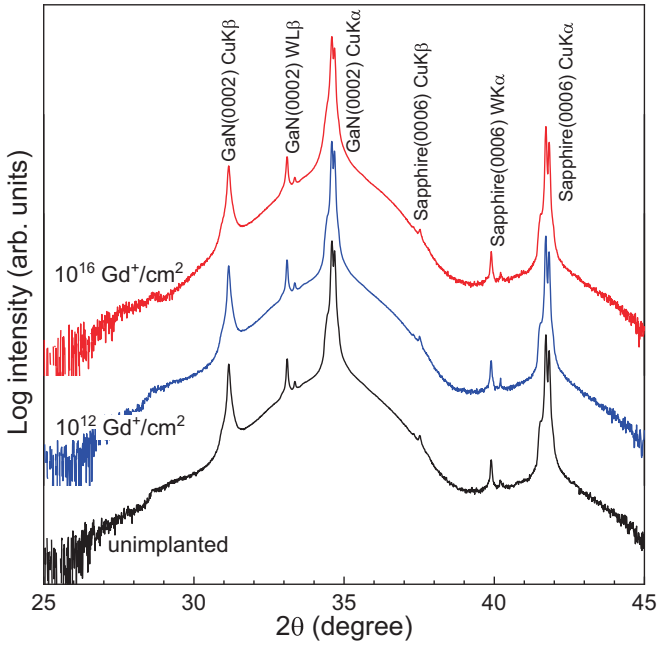

FIG. 4. The XRD spectra for the unimplanted sample and the implanted samples with the doses of $\phi = 10^{12}$ and 10^{16} Gd^+/cm^2 after annealing at 900° C.

B. Magnetic property by SQUID

Figures 5(a) to 5(d) show the *M–H* curves obtained at 10 and 300 K for the unimplanted sample and all the implanted samples before and after annealing at 900° C. In the unimplanted state, hysteresis is almost null or very weak. That is, this is the level of artificial response of SQUID apparatus and/or magnetic contamination during sample handling. After implantation, the saturation magnetization clearly increases to nearly the same level except for $\phi = 10^{16}$ Gd^+/cm^2, and decreases slightly from 10 to 300 K. After annealing at 900° C, the saturation magnetization starts to increase from $\phi = 10^{12}$ Gd^+/cm^2 and saturates at the level higher than that for the as-implanted states at $\phi \geqslant 10^{13}$ Gd^+/cm^2.

The dose dependence of *M–H* curve after annealing seems to be systematic. However, one may feel that the dose dependence in the as-implanted state is peculiar. That is, the saturation magnetization only for $\phi = 10^{16}$ Gd^+/cm^2 is lost and that for $\phi = 10^{12}$ Gd^+/cm^2 is higher even without annealing. For $\phi = 10^{16}$ Gd^+/cm^2, it is speculated that heavy irradiation damage and/or extremely high Gd concentration (supersaturation) prohibit the appearance of magnetization in the as-implanted state, while damage recovery and dispersion of Gd atoms upon annealing result in a finite magnetization. For $\phi = 10^{12}$ Gd^+/cm^2, it is speculated that the defect concentration is appropriate to assist the magnetization in the as-implanted state, while upon annealing the defect concentration decreases and the magnetization is lost.

As shown in Fig. 5(e), the annealed samples exhibit hysteresis loops. (The curve for $\phi = 10^{12}$ Gd^+/cm^2 is not plotted since the saturation magnetization is small.) The coercivity is estimated to be approximately 150 Oe. In the as-implanted states, such hysteresis loops were not clearly seen.

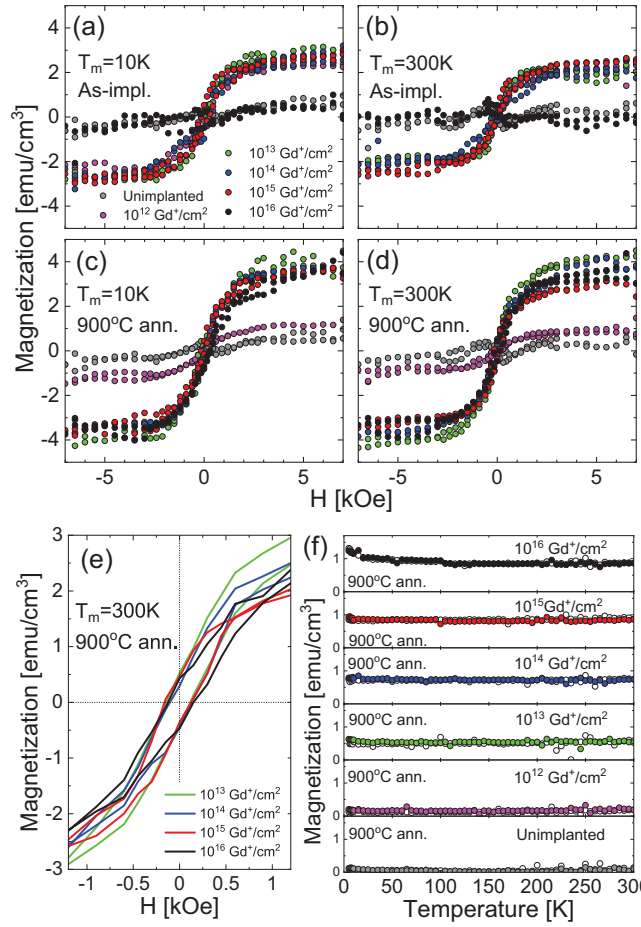

FIG. 5. (a)–(d) *M*−*H* curves measured at 10 and 300 K for all the Gd-implanted samples in the as-implanted states and after annealing at 900° C for 30 min (solid circles) and the unimplanted sample (grey circles). (e) Magnification of *M*−*H* curves for the implanted samples after 900° C for 30 min measured at 300 K. (f) *M–T* curves for the implanted samples after 900° C for 30 min in the field cooling (filled circles) and zero-field cooling (open circles) conditions at 200 Oe.

Figure 5(f) shows the *M–T* curves obtained for the implanted samples after annealing at 900° C. Overall, the magnetization level increases from the unimplanted state to the highest dose systematically. Also, the magnetization increases slightly at low temperature implying the existence of paramagnetic component. But, as expected from the comparable magnetizations at 10 and 300 K in *M–H* curves, the magnetization is almost independent of temperature. This implies that the magnetic phase transitions occur above 300 K. The difference between the field-cooling and zero-field cooling conditions is not seen, suggesting the absence of superparamagnetic component. The temperature dependencies arising from secondary GdN and metal Gd phases are not seen either. This is consistent with the XRD observation in Fig. 4.

Figure 6 shows the effective magnetizations per Gd atom obtained before and after annealing at 900° C. These vary from ∼3000 μ_B/Gd for $\phi = 10^{12}$ Gd^+/cm^2 to below 1 μ_B/Gd for $\phi = 10^{16}$ Gd^+/cm^2.

The above results may allow us to conclude that ferromagnetism is induced in the Gd-implanted GaN samples and

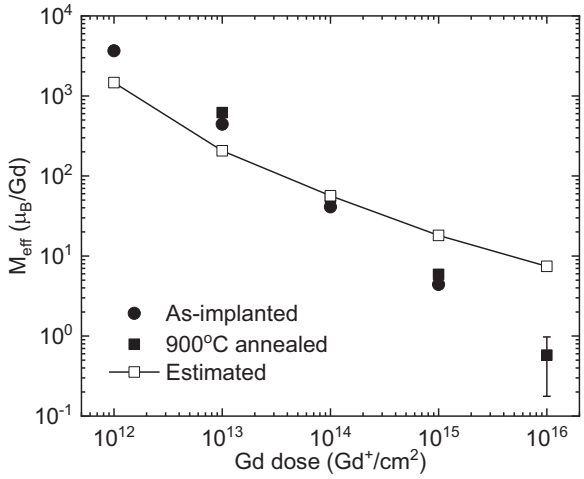

FIG. 6. The effective magnetization per implanted Gd atom obtained in the as-implanted state (solid circles) and after annealing at 900° C for 30 min (solid squares). The estimated values with the concentration of vacancy clusters after annealing and assumed magnetization per vacancy cluster are plotted as open squares.

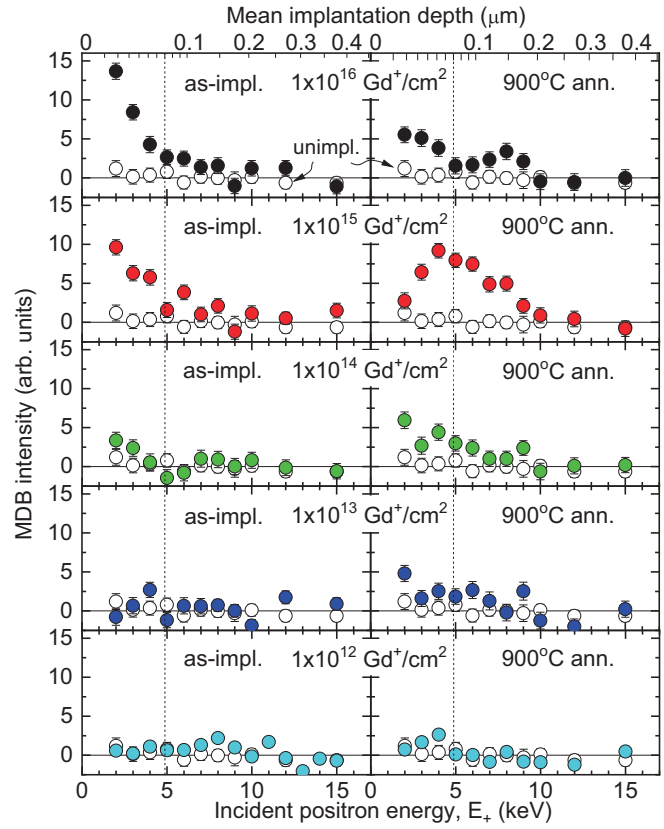

FIG. 7. Plots of magnetic Doppler broadening (MDB) intensity versus incident positron energy at 300 K (filled circles) for the Gd-implanted samples before and after annealing at 900° C for 30 min (filled circles) and for the unimplanted sample (open circles). The upper horizontal axes show the mean positron implantation depth. Dashed lines denote the mean Gd range.

it is colossal. However, it is known that, apart from simple magnetic contamination of sample, the SQUID magnetometry creates some serious artifacts, such as spurious magnetization and ferromagnetic loop mainly due to the pinning of magnetic flux [16,17]. Unfortunately, there are no definitive ways to judge if the observed features arise from genuine ferromagnetism or just fakes. It is said that in early studies, these risks involving the SQUID magnetometry were not well known and the so-called colossal magnetism of GaN:Gd was claimed. Therefore, at this moment, we can only suspend the argument for the existence of ferromagnetism.

C. Vacancy spin by SP-PAS

Figure 7 shows plots of the MDB intensity versus E_+ at 300 K for all the samples. Nearly the same features were obtained at 20 K, indicating no temperature dependence. For the unimplanted sample, no finite MDB intensities were found, suggesting that electrons participating in the positron annihilation are not spin-polarized. In the as-implanted states, finite MDB intensities are seen only for $\phi = 10^{15}$ and 10^{16} Gd$^+$/cm^2 at $E_+ \leqslant 5$ keV. Considering the fact that vacancy clusters are formed there as shown in Fig. 2, such vacancy clusters are probably spin-polarized. After annealing, the MDB intensities at $E_+ \leqslant 5$ keV are reduced considerably. Instead, the MDB intensities at around $E_+ = 5$ keV (around the Gd range) increase with increasing dose from $\phi = 10^{13}$ to 10^{15} Gd$^+$/cm^2. The MDB intensity for $\phi = 10^{16}$ Gd$^+$/cm^2 is still nonzero but is suppressed considerably. The MDB intensity for $\phi = 10^{12}$ Gd$^+$/cm^2 is under the detection limit. Again, the increase (decrease) of the MDB intensity seems to coincide with the appearance (disappearance) of vacancy clusters as discussed in the *S*–*E* plots in Fig. 2.

Figure 8 shows the MDB differential spectrum $N_+(p) - N_-(p)$ at 300 K for the implanted sample with $\phi = 10^{15}$ Gd$^+$/cm^2 after annealing at 900°. The data for $E_+ = 4-6$ keV are integrated for better statistics. The spectrum has an upward peak at its center. In the context so far, the problem is if this spectrum feature can be explained considering V_{12} clusters. The present calculations showed that small vacancy defects (V_{Ga}, V_N, $V_{Ga}V_N$) have spontaneous magnetizations (3, 1, 2 μ_B, respectively) irrespective of the presence of Gd atoms. However, V_{12} has no magnetization in the supercell without a Gd atom. We therefore further calculated (i) with the Gd-added supercell including separated Gd atom and V_{12}, and (ii) with the clean supercell including two close V_{12} clusters separated by an interatomic distance to mimic the high density condition. The first induced no magnetization on the V_{12} cluster, while in the second case spontaneous magnetization of 2 μ_B/V_{12} appeared due to the formation of partially filled states. As seen in Fig. 8, the calculated spectrum for V_{Ga} has a downward peak at the centers, which is because of the preferential annihilation of positrons with spin-polarized N valence electrons. Such a downward-peak spectrum hardly explains the experimental upward-peak spectrum. Contrarily, V_N and V_{12} give rise to upward-peak spectra because of the spin polarization of Ga valence electrons. The MDB intensity of V_N is not sufficient because of the weak localization of the positron wave function and thus is not comparable to the experiment. Both the intensity and curve shape of V_{12} are comparable to the experiment. Thus, spin-polarized V_{12}

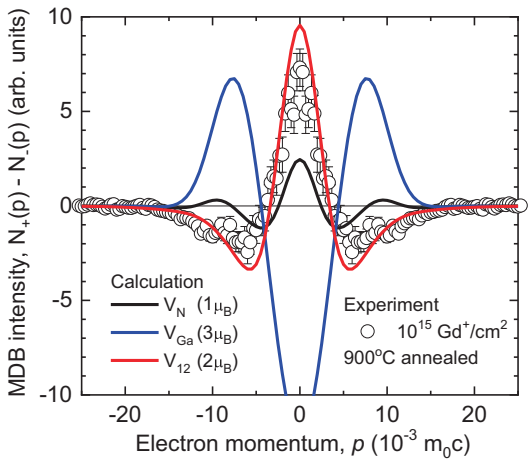

FIG. 8. MDB spectrum measured at 300 K for the Gd-implanted sample with a dose of 10^{15} cm^{-2} after annealing at 900° C (open circles). The data for 4–6 keV were summed for better statistics. The solid curves denote the theoretical calculations assuming V_N (black), V_{Ga} (blue), and V_{12} (red) cluster.

clusters may be the major positron trapping centers. This is consistent with the discussion based on the ratio DBAR curve in Fig. 3.

V. DISCUSSION

The present observations and their interpretations by the calculation are summarized in Table I.

In the as-implanted low dose conditions, single Ga vacancies were detected as the major positron trapping centers (Fig. 3). However, SP-PAS measurements showed no spin polarization on single Ga vacancies (Fig. 7). Therefore, if the observed magnetizations in Fig. 5 are genuine, those are not mediated by single Ga vacancies. It is possible that the other mechanisms need to be considered. In the present calculation, single N vacancy also possesses a magnetization of 1 μ_B. Some other point defects such as interstitials and antisites may also induce magnetizations [35]. To clarify such possibilities further study is needed.

In the as-implanted high-dose condition, vacancy clusters at least larger than V_{12} were formed in the regions shallower than the mean Gd range (Figs. 2 and 3). These vacancy clusters were found to be spin-polarized (Fig. 7). Therefore, if the observed magnetizations in Fig. 5 are genuine, those may be explained considering large vacancy clusters. However, the highest dose, i.e., $\phi = 10^{16}$ Gd$^+$/cm^2, is exceptional since no magnetization appeared (Fig. 5).

Upon post-implantation annealing, small vacancies disappeared. Instead, vacancy clusters larger than at least V_{12} were formed as the predominant defect species even in the lowest dose, i.e., $\phi = 10^{12}$ Gd$^+$/cm^2 (Fig. 3). Based on the argument of the number of dangling bonds, V_{12} may be energetically stable [36]. This may be why such vacancy clusters form upon post-implantation annealing. Because the experimental DBAR spectrum for $\phi = 10^{15}$ Gd$^+$/cm^2 after annealing coincides with the nonrescaled theoretical curve for V_{12}, injected most positrons are probably trapped by vacancy clusters. Thus, the concentration of vacancy clusters should be very high $\gtrsim 10^{19}$ cm^{-3}. In the SRIM simulation, each Gd ion creates approximately 4500 vacancies. Therefore, even if many Frenkel pairs recombine immediately during irradiation, an extremely high concentration of vacancy clusters may be formed. The spin-polarizations associated with these vacancy clusters were detected except for the lowest dose, i.e., $\phi = 10^{12}$ Gd$^+$/cm^2 (Fig. 7). Therefore, if the observed magnetizations in Fig. 5 are genuine, those may be explained as mediated with vacancy clusters.

One may think the effect of Gd decoration on the spin polarization of V_{12}. We examined such effects and found that by decorating V_{12} with a Gd atom, no spin-polarizations are induced except for the spin-polarization of Gd atom itself. The experimental MDB spectrum was also not reproduced considering the Gd decoration. Even if some spin polarizations are induced with Gd decoration, the colossal ferromagnetism (if it exists) is hardly explained, since the colossal ferromagnetism needs some magnetic species other than Gd itself that mediate ferromagnetism.

Assuming that vacancies and Gd atoms cause a macroscopic magnetization, the effective magnetization per Gd may be given by $C_V M_V / N_{Gd} + 7\,\mu_B$, where C_V is the vacancy concentration, M_V is the magnetization associated with a vacancy, and N_{Gd} is the concentration of implanted Gd. The vacancy concentration is given by $C_V = f\lambda_B/[\mu(1-f)]$, where μ is the positron trapping coefficient of the vacancy, λ_B is the positron annihilation rate in the bulk, and f is the fraction of positrons trapped by vacancies and given by $f = (S - S_B)/(S_V - S_B)$, where S_B and S_V are the intrinsic S parameters for the bulk and vacancy. One may take $S_B = 0.463$ and $S_V = 0.541$ from Fig. 2, and the theoretical $M_V = 2\ \mu_B$ for V_{12} and $\lambda_B = 6$ ns^{-1} from the literature [37]. Normally, μ is of the order of 10^{14} s^{-1} in either the transition-limited regime or the diffusion-limited regime. In the diffusion-limited regime, μ is given by $4\pi R D_+ / N_A$, where R is the effective positron

TABLE I. Summary of experimental observations and interpretations by calculation.

Dose	As-implanted			900° C annealed		
(Gd$^+$/cm^2)	Magnetization	Vacancy spin	Defect species	Magnetization	Vacancy spin	Defect species
10^{16}	Invisible	Exist	Vacancy clusters	Exist	Exist	Vacancy clusters
10^{15}	Exist	Exist	Vacancy clusters	Exist	Exist	Vacancy clusters
10^{14}	Exist	Weak	Vacancy clusters, small vacancies	Exist	Exist	Vacancy clusters
10^{13}	Exist	Invisible	Small vacancies, V_{Ga} etc	Exist	Exist	Vacancy clusters
10^{12}	Exist	Invisible	Small vacancies, V_{Ga} etc	Weak	Invisible	Vacancy clusters

trapping radius of vacancy (approximate geometrical size of vacancy, i.e., a few Å in the present case), D_+ is the positron diffusion constant, and N_A is the atomic density. In the positron diffusion in a clean matrix with phonon scattering, D_+ is approximately 1 cm^2/s. However, in the defective matrix due to the radiation damage, the positron diffusion may not be necessarily the same as that in clean matrix due to the scattering by defects [38]. If we take one order of magnitude smaller diffusion constant, then the effective magnetization per Gd was drawn in Fig. 6. It seems that the dose dependence of effective magnetization can roughly be explained.

VI. CONCLUSION

The defect-assisted magnetism in Gd-implanted GaN is still far from full understanding. One reason is that in the detection of electron spins associated with defects, the potential methods have been limited. In this study, we applied the SP-PAS method for Gd-implanted GaN. The electrons associated with larger vacancy clusters were found to be spin-polarized. Such spin-polarized vacancy clusters may be the source of ferromagnetism. However, the SQUID magnetometry has a serious problem in manifesting the existence of ferromagnetism. In this respect, the improvement of SQUID magnetometry and the development of alternative methods are indispensable.

ACKNOWLEDGMENTS

This work was supported, in part, by JSPS KAKENHI under Grant No. 18K04931.

[1] H. Ohno, H. Munekata, T. Penney, S. von Molnár, and L. L. Chang, Phys. Rev. Lett. **68**, 2664 (1992).
[2] H. Ohno, A. Shen, F. Matsukura, A. Oiwa, A. Endo, S. Katsumoto, and Y. Iye, Appl. Phys. Lett. **69**, 363 (1996).
[3] K. Olejnik, M. H. S. Owen, V. Novak, J. Masek, A. C. Irvine, J. Wunderlich, and T. Jungwirth, Phys. Rev. B **78**, 054403 (2008).
[4] T. Dietl, H. Ohno, F. Matsukura, J. Cibert, and D. Ferrand, Science **287**, 1019 (2000).
[5] N. Teraguchi, A. Suzuki, Y. Nanishi, Y.-K. Zhou, M. Hashimoto, and H. Asahi, Solid State Commun. **122**, 651 (2002).
[6] S. Dhar, O. Brandt, M. Ramsteiner, V. F. Sapega, and K. H. Ploog, Phys. Rev. Lett. **94**, 037205 (2005).
[7] S. Dhar, L. Pérez, O. Brandt, A. Trampert, K. H. Ploog, J. Keller, and B. Beschoten, Phys. Rev. B **72**, 245203 (2005).
[8] L. Pérez, G. S. Lau, S. Dhar, O. Brandt, and K. H. Ploog, Phys. Rev. B **74**, 195207 (2006).
[9] S. Dhar, T. Kammermeier, A. Ney, L. Pérez, K. H. Ploog, A. Melnikov, and A. D. Wieck, Appl. Phys. Lett. **89**, 062503 (2006).
[10] S. Y. Han, J. Hite, G. T. Thaler, R. M. Frazier, C. R. Abernathy, S. Pearton, H. K. Choi, W. O. Lee, Y. D. Park, J. M. Zavada, and R. Gwilliam, Appl. Phys. Lett. **88**, 042102 (2006).
[11] M. A. Khaderbad, S. Dhar, L. Pérez, K. H. Ploog, A. Melnikov, and A. D. Wieck, Appl. Phys. Lett. **91**, 072514 (2006).
[12] J. Hejtmánek, K. Knížek, M. Maryško, Z. Jirák, D. Sedmidubský, Z. Sofer, V. Peřina, H. Hardtdegen, and C. Buchal, J. Appl. Phys. **103**, 07D107 (2008).
[13] R. P. Davies, B. P. Gila, C. R. Abernathy, S. J. Pearton, and C. J. Stanton, Appl. Phys. Lett. **96**, 212502 (2010).
[14] Z. Sofer, D. Sedmidubský, M. Moram, A. Macková, M. Maryško, J. Hejtmánek, C. Buchal, H. Hardtdegen, M. Václavů, V. Peřina, R. Groetzschel, and M. Mikulics, Thin Solid Films **519**, 6120 (2005).
[15] S. Shvarkov, A. Ludwig, A. D. Wieck, Y. Cordier, A. Ney, H. Hardtdegen, A. Haab, A. Trampert, R. Ranchal, J. Herfort, H. Becker, D. Rogalla, and D. Reuter, Phys. Status Solidi B **251**, 1673 (2014).
[16] M. Sawicki, W. Stefanowicz, and A. Ney, Semicond. Sci. Technol. **26**, 064006 (2011).
[17] M. Buchner, K. Höfler, B. Henne, V. Ney, and A. Ney, J. Appl. Phys. **124**, 161101 (2018).
[18] A. Ney, T. Kammermeier, V. Ney, S. Ye, K. Ollefs, E. Manuel, S. Dhar, K. H. Ploog, E. Arenholz, F. Wilhelm, and A. Rogalev, Phys. Rev. B **77**, 233308 (2008).
[19] A. Ney, T. Kammermeier, K. Ollefs, V. Ney, S. Ye, S. Dhar, K. H. Ploog, M. Röver, J. Malindretos, A. Rizzi, F. Wilhelm, and A. Rogalev, J. Magn. Magn. Mater. **322**, 1162 (2010).
[20] A. Ney, Materials **3**, 3565 (2010).
[21] P. Dev, Y. Xue, and P. Zhang, Phys. Rev. Lett. **100**, 117204 (2008).
[22] O. Volnianska and P. Boguslawski, Phys. Rev. B **83**, 205205 (2011).
[23] P. Dev and P. Zhang, Phys. Rev. B **81**, 085207 (2010).
[24] L. Liu, P. Y. Yu, Z. Ma, and S. S. Mao, Phys. Rev. Lett. **100**, 127203 (2008).
[25] Y. Gohda and A. Oshiyama, Phys. Rev. B **78**, 161201(R) (2008).
[26] M. Roever, J. Malindretos, A. Bedoya-Pinto, A. Rizzi, C. Rauch, and F. Tuomisto, Phys. Rev. B **84**, 081201(R) (2011).
[27] M. Maekawa, H. Abe, A. Miyashita, S. Sakai, S. Yamamoto, and A. Kawasuso, Appl. Phys. Lett. **110**, 172402 (2017).
[28] J. F. Ziegler, J. P. Biersack, and M. D. Ziegler, *The Stopping and Range of Ions in Matter* (SRIM Co., Chester, Maryland, 2008).
[29] M. J. Puska and R. M. Nieminen, Rev. Mod. Phys. **66**, 841 (1994).
[30] P. E. Blöchl, Phys. Rev. B **50**, 17953 (1994).
[31] X. Gonze, J.-M. Beuken, R. Caracas, F. Detraux, M. Fuchs, G.-M. Rignanese, L. Sindic, M. Verstraete, G. Zerah, F. Jollet, M. Torrent, A. Roy, M. Mikami, P. Ghosez, J.-Y. Raty, and D. Allan, Comput. Mater. Sci. **25**, 478 (2002).
[32] A. Thiess, P. H. Dederichs, R. Zeller, S. Blügel, and W. R. L. Lambrecht, Phys. Rev. B **86**, 180401(R) (2012).

[33] E. Clementi and C. Roetti, At. Data Nucl. Data Tables **14**, 177 (1974).
[34] E. Boroński and R. M. Nieminen, Phys. Rev. B **34**, 3820 (1986).
[35] H. Li, M. Maekawa, A. Miyashita, and A. Kawasuso, Defect Diffusion Forum **373**, 65 (2017).
[36] A. Yabuuchi, M. Maekawa, A. Kawasuso, Y.-K. Zhou, S. Hasegawa, and H. Asahi, Appl. Phys. Lett. **102**, 142406 (2013).
[37] R. Krause-Rehberg and H. S. Leipner, *Positron Annihilation in Semiconductors* (Springer, New York, 1998).
[38] W. Brandt, Appl. Phys. **5**, 1 (1974).